Journal of Materiomics 9 (2023) 1129–1140

Contents lists available at ScienceDirect

Journal of Materiomics

journal homepage: www.journals.elsevier.com/journal-of-materiomics/

Research paper

MXene: An efficient hemoperfusion sorbent for the removal of uremic toxins

Tianyi Wang [a], Wei Gu [a], Lu Yu [a], Xin Guo [b], Jian Yang [a], Xiaoyu Sun [a], Jun Guan [c], Lin Zhou [c], Chengyin Wang [a], Hang Yao [a, **], Xiuyun Zhang [d, ***], Guoxiu Wang [b, *]

[a] College of Chemistry and Chemical Engineering, Yangzhou University, Yangzhou, 225000, Jiangsu Province, China
[b] Centre for Clean Energy Technology, School of Mathematics and Physics, Faculty of Science, University of Technology Sydney, Broadway, Sydney, NSW2007, Australia
[c] Clinical Medical College, Su Bei People's Hospital, Yangzhou University, Yangzhou, 225000, Jiangsu Province, China
[d] College of Physical Science and Technology, Yangzhou University, Yangzhou, 225000, Jiangsu Province, China

ARTICLE INFO

Article history:
Received 24 March 2023
Received in revised form
8 June 2023
Accepted 18 June 2023
Available online 7 July 2023

Keywords:
2D materials
MXene
Hemoperfusion
Middle molecular weight toxin
Protein bound toxin
Adsorption

ABSTRACT

MXene, a family of two-dimensional (2D) transition metal carbides and nitrides have attracted extensive interests for many biochemical applications, including tumour elimination, biosensors, and magnetic resonance imaging (MRI). In this article, we firstly discovered that $Ti_3C_2T_x$ MXene exhibited a highly efficient adsorption capability as hemoperfusion absorbent towards middle-molecular mass and protein bound uremic toxins in the end stage of renal disease (ESRD) treatment. Molecular scale investigations reveal that the high efficiency of MXene for the removal of uremic toxins could be attributed to synergistic effects of physical/chemical adsorption, electrostatic interaction surface of 2D MXene, and transformation of protein secondary structure. 2D MXene materials could be used as a new hemoperfusion sorbent with ultrahigh efficiency for removing uremic toxins during the treatment of kidney disease.

1. Introduction

In the 21st century, chronic kidney disease (CKD) has become the sixth fastest growing disease in the world [1]. Until now, more than 850 million people worldwide are suffering from CKD. When these patients reach the end stage of renal disease (ESRD), their kidneys only can function at 10%–15% of the normal capacity [2]. To prolong their life spans, most ESRD patients normally have two options: one is continuous renal replacement therapy (CRRT), and another is kidney transplantation [3]. However, only extremely limited number of patients have precious opportunities to receive kidney transplant surgery because of scarcity source of replacement kidney, biological incompatibility and the prohibitive cost [3]. Thus, CRRT has to be the only choice for most ESRD patients.

To date, modern CRRT can be classified into two methods: hemodialysis and hemoperfusion [4]. Hemodialysis has been widely known as using semipermeable membranes contained in the dialysate column to remove small molecular weight harmful substances such as urea, uric acid and creatine [5]. The modern hemodialysis technology has met the strict requirements for the clearance of most small molecular harmful substances. However, except for small molecular mass harmful substances (more than 90 kinds of common toxins have been recognized in blood of ESRD patients), middle molecular mass molecules (between 500 and 1,200 Da, such as indole sulphate) and protein bound toxic content (β2-microglobulin *etc.*) are also detrimental to the health of ESRD patients [6]. Owing to large molecular mass, these two kinds of toxic content cannot cross the pores of the semipermeable membrane, thus cannot be removed by hemodialysis.

Hemoperfusion has been widely regarded as a complementary technique to overcome the shortcomings of hemodialysis in clinical treatment, which can directly remove toxins in blood by using absorbent materials [7]. Unlike hemodialysis, hemoperfusion uses special absorbent to directly adsorb toxins in the blood. In most

* Corresponding author.
** Corresponding author.
*** Corresponding author.
E-mail addresses: yaohang@yzu.edu.cn (H. Yao), xyzhang@yzu.edu.cn (X. Zhang), guoxiu.wang@uts.edu.au (G. Wang).
Peer review under responsibility of The Chinese Ceramic Society.

https://doi.org/10.1016/j.jmat.2023.06.010

clinical treatments, hemoperfusion and hemodialysis are employed together in series. Hemoperfusion is especially very important for patients suffering from acute hemotatoxicosis. For most uremic patients, even when maintaining dialysis at a frequency for 1–3 times a week, they still need hemoperfusion therapy for several times per year. For the treatment of novel coronavirus (COVID-19) patients, hemoperfusion is also considered as an irreplaceable and effective approach to eliminate inflammatory factors such as interleukin-6 (a kind of protein bound toxin) and alleviate "cytokine storm" during the rescue of severe COVID-19 patients [8].

At present, the common commercial hemoperfusion absorbents are usually made of active carbon (AC) and resin. However, these traditional absorbents have low removal efficiency, which cannot meet the rapidly increasing demands for the treatment of ESRD patients [9]. Therefore, it is imperative to develop new hemoperfusion adsorbents with high efficiency and broad-spectrum adsorption function towards all kinds of toxins (*e.g.* small-, middle-molecular weight and protein bound toxins). MXenes, a new type of two-dimensional transition metal carbides, carbonitrides and nitrides, have attracted extensive interests in diverse domains [9] such as electrochemistry [10], biochemistry [11] and electronics [12] *etc*. MXenes represent by a general formula of $M_{n+1}X_nT_x$ (n = 1–3), where M is an early transition metal, X is carbon and/or nitrogen, and T_x denotes the hydroxyl/oxy/fluoride surface terminations [13]. The physico-chemical properties and surface functional groups of MXenes are tunable by varying their precursor MAX compositions and the type of etching (hydrofluoric acid concentration and/or mixed acid composition), which endows the derived MXenes with abundant physical and chemical characteristics [14]. Particularly, the functionalization of surfaces not only enables MXenes to be hydrophilic, but also empowers MXenes with superior adsorption capability to various chemical molecules [15]. Their unique 2D ceramic packaging structure makes MXene the first to be well applied in energy storage and electrochemistry [16–18]. Previously, the MXene has become an ideal in various domains, such as CO_2 capture [19], toxic NH_3 gas adsorption [20], water purification [21], and even radioactive pollutant removal [22]. This is mainly due to the large specific surface area and abundant surface polar functional groups of MXene. Recently, Meng et al. have demonstrated the positive effects of MXenes for adsorbing urea, which is one kind of small molecular weight toxins from kidney disease patients' waste dialysate [23]. However, there is still no efficient absorbent for removing middle-molecular weight and protein-bound toxins, hindering the effective treatment for patients suffering from kidney failure.

According to our previous research, we found that MXene has excellent removal ability towards interleukin 6 (IL-6) [24] and bilirubin [25], herein, for the first time, we systematically analyze $Ti_3C_2T_x$ MXene as an adsorbent in hemoperfusion for three kinds of common uremic toxins (*e.g.*, small-; middle-molecular weight toxin and protein bound toxin) We especially focus on its removal capability towards middle-molecular weight and protein-bound toxins. High resolution transmission electron microscopy (HR-TEM) and X-ray photoelectron spectroscopy (XPS) were employed cooperatively to illustrate details of toxin adsorption process. MXene absorbent can efficiently remove toxins in real blood of ESRD patients without breaking balance of positive blood composition, which has been confirmed by analyses using Roche Automatic Biochemical Immunoanalyzer.

2. Experimental section

2.1. Preparation of MXene adsorbent

Ti_3AlC_2 with a particle size of <38 μm was synthesized according to the previous report [13]. Then, 3 g of as-prepared Ti_3AlC_2 powder was etched in a mixture of 3 g lithium fluoride (LiF, Alfa Aesar) and 30 mL 9 mol/L hydrochloric acid (HCl, Fisher Scientific) at ~35 °C for 24 h to extract the Al atoms and obtain multilayered $Ti_3C_2T_x$ suspension. The obtained suspension was repeatedly rinsed with distilled water and centrifuged (3,500 r/min) until the pH of the supernatant was higher than 5.

2.2. Preparation of PAN electrospinning membrane

In a typical electrospinning procedure of PAN membrane, a solution of 9% (in volume) PAN powder (MW150,000, Macklin, Shanghai) in N, N-Dimethylformamide (DMF) (AR, Macklin, Shanghai) was prepared in the temperature of 37 °C. After stirred for 10 h, the solution was allowed to stand for 10 min. The fiber was spun at an electric field of 20.00 kV with a feeding rate of 0.1 mm/min from a 23-gauge needle (SS–2535H, Yongkang, Shanghai). An Al foil was employed as a collector and the distance between needle and collector was 15 cm. Spinning temperature was maintained at 25–30 °C and the humidity was kept at 45%–50%. After the spinning, the interlayer was exfoliated from the collector and heated in a vacuum oven at 100 °C for 6 h.

2.3. Adsorption experiment

Lysozyme (Biotechnology grade, Macklin, Shanghai, China); Vitamin B-12 (98%, Macklin, Shanghai, China). MXene adsorption experiments of both lysozyme and vitamin B-12 were all carried out from aqueous solution under ambient temperature. MXene adsorbent of 5 different qualities (2.0, 4.0, 8.0, 16.0 mg and 32.0 mg) was added into 4 mL lysozyme solution. The solution was centrifuged for 10 min at 10,000 r/min and then, the solution stood for peace. UV–visible–near infrared absorption spectrometer (Cary 5000, Varian, USA) was used to monitor the concentration of the lysozyme and VB-12. The adsorption experiment to β-microglobulin was conducted in Northern Jiangsu hospital, Yangzhou, China. The concentration of β-microglobulin and other components in real blood was characterized by an Automatic biochemical immune analyzer (Cobas 8000, Roche Diagnostics GmbH, Germany) while the collection of blood samples was approved by patients.

2.4. Characterizations

After adsorption of toxin molecules on MXene was characterized by Fourier Transform Infrared Spectrometer (FTIR) (Nicolet 6700 Spectrometer), Circular dichroism spectra (J-810, JASCO Company, Japan), Nuclear magnetic resonance (NMR) (AVANCE 600, Bruker, Germany), X-ray photoelectron spectroscopy (XPS) (ESCALAB250Xi, and ThermoFisher Scientific, USA). The MXene/lysozyme mixed solution was centrifugal for 10 min at 10,000 r/min. The sediment was freeze dried before SEM characterization. High resolution transmission electron microscopy (HR-TEM) was operated at 300 kV electron microscope (Tecnai G2 F30 S-TWIN, FEI). The low concentrated MXene@LYZ solution was dropped on the copper mesh (400) and dried for 10 min before the characterization. CD spectra of lysozyme were collected on a Jasco spectropolarimeter, model 810, with a quartz cell of 10 mm path length for near-UV. The concentration of lysozyme was 20–40 μmol/L in the solution of deionized water. To prevent CD intensity from changing with temperature, it is necessary to use cooling water (flow rate 2.0 L/min) for the light source (Xe light).

2.5. DFT calculation

All the calculations were performed in the framework of spin

polarized DFT as implemented in the Vienna *ab-initio* Simulation Package (VASP) [26]. The exchange-correlation potentials were treated by the generalized gradient approximation (GGA) parameterized by Perdew, Burke and Ernzerholf (PBE) [27,28]. The interaction between valence electrons and ion cores was described by the projected augmented wave (PAW) method [29], and DFT-D2 method [30] considering van der Waals (vdW) interaction was adopted for the TM-C_{60} systems. The electronic wave functions were expanded in a plane-wave basis with a cutoff energy of 400 eV. The vacuum region between wires was set to 15 Å and the reciprocal space was sampled by 1 × 1 × 1 grid meshes using the Monkhorst-Pack scheme for geometry optimization [31]. All the atoms were fully relaxed until the Hellmann-Feynman force on each atom was less than 0.01 eV/Å.

2.6. In vivo whole blood perfusion

The animal study was approved by the Ethics Committee for Experimental Animals of Yangzhou University (Yangzhou China), and the work was in compliance with the National Institutes of Health Guidelines for the Care and Use of Laboratory Animals (NIH Publications No. 8023, revised 1978). The process was carried out at a stable temperature of 38.8 °C, with a flow rate of 30 mL/min for 30 min. The vivo whole blood perfusion experiment was carried out in college of Veterinary Medicine Yangzhou University.

3. Results and discussion

3.1. $Ti_3C_2T_x$ MXene nanosheets preparation and characterizations

$Ti_3C_2T_x$ MXene nanosheets were prepared by exfoliating Ti_2AlC_2 MAX phase precursors *via* a conventional acid-etching procedure using hydrofluoric acid to remove Al layer [11]. The morphology of the as-prepared MXene material was characterized by scanning electron microscopy (SEM) and transmission electron microscopy (TEM). As shown in Fig. 1a, just after the etching process, these pristine MXene nanosheets emerge as an accordion-like superposed aggregation. These multilayer MXene nanosheets were furtherly exfoliated *via* sonication process, centrifuged at high speed and washed for several times to obtain a few-layered pure $Ti_3C_2T_x$ dispersions in deionized water (as shown in the inset of Fig. 1b and Fig. S1). The TEM image reveals that the exfoliated MXene nanosheets is ultrathin in thickness with a large lateral size, which endows MXene with abundant active sites for toxin adsorption (Fig. S2).

The high-resolution TEM (HR-TEM) image demonstrates the atomic structure of as-synthesized MXene material, in which three layers of Ti atoms can be clearly identified with an interlayer distance of 1.5 nm (Fig. 1c). The (001) peak in the XRD pattern corresponding to $Ti_3C_2T_x$ nanosheet became broader and shifted to lower angles, which is consistent with the HR-TEM results (Fig. S3). The energy-dispersive X-ray spectroscopy (EDS) mapping identifies the elementary composition of MXene nanosheets with C, Ti, O and F (Fig. S4). The external chemistries of $Ti_3C_2T_x$ MXene were characterized by the XPS analysis, demonstrating that the MXene surfaces are mainly terminated with hydrophobic (−F) and, hydrophilic (−OH, =O) functional groups (see details in Fig. S5). Fig. 1d illustrates the designed hemoperfusion process using MXene adsorbent to remove uremic toxins. The strong physical and chemical adsorption abilities contributed from abundant functional groups on MXene surface can effectively immobilize toxin molecules. The high efficiency removal performance can guarantee purified blood reinjected the patient's body with low uremic toxin concentration. Density functional theory calculations (DFT) were performed to identity the adsorption properties of $Ti_3C_2T_x$ MXene towards the typical protein bound toxins. Here, lysozyme (LYZ) was chosen as a representative protein bound toxins because of its similar chemical and physical properties to other toxins in patients' blood (Table S1) [32]. In order to reduce the computational complexity, we selected three characteristic amino acid segments of LYZ, which are denoted as Fragment A, B and C, respectively (as shown in Fig. S6). The nine possible interactions (3 × 3) between the three LYZ segments and $Ti_3C_2T_x$ MXenes with three possible surface terminations (−OH, −O−, or −F) were simulated and quantified by the adsorption binding energies (E_b) (Fig. 2). Generally, MXene showed excellent adsorption ability to LYZ and the computed binding energies vary from -9.86 to -1.46 eV depending on MXene structures and the target LYZ segments. Although the −O− and −OH terminated MXenes show strong adsorption strength for the LYZ toxin, the most stable adsorption combination are from the −F terminated MXene with binding energies of -9.86, -9.38 eV and -8.6 eV to A, B and C segments, respectively. Since the F- group consists of about 1/2 of all terminal groups (calculated from the result of XPS), it can significantly improve the adsorption capacity of MXene absorbents to protein bound toxins. Furthermore, we investigated the charge density differences (CDD) between various toxin segments and functionalized $Ti_3C_2T_x$ surfaces. As shown in Fig. 2j, the −O− terminated MXene has the largest charge transfer (1.18 e−0.45 e). While the −OH terminated MXene has the lowest values (0.09 e − 0.03 e). Such significant CDDs between the $Ti_3C_2T_x$ surface and various LYZ segments could contribute the strong interaction between MXene and toxin segments.

3.2. $Ti_3C_2T_x$ MXene adsorptions performances

To validate the theoretical calculations, we examined the adsorption capability of $Ti_3C_2T_x$ MXene for removing the middle-molecular weight toxins and protein-bound toxins from aqueous solution. In addition to the LYZ toxin, we also chose vitamin B-12 (VB12, with a molecular weight of 1355 Da) as a representative of the middle-molecular weight toxins (Fig. S7 shows its molecular structure). Due to the same molecular weight and similar chemical composition, VB12 is appointed as a representative substance for evaluating new hemoperfusion absorbents [30]. Ultraviolet−Visible (UV) spectroscopy was used to quantitatively detect the decrease of concentration of LYZ and VB12. Other typical toxins, such as urea and uric acid, were also analyzed by a Roche Automatic Biochemical Immunoanalyzer (Fig. S8). Commercial activated carbon (AC) sorbent (coconut shell carbon), which has been widely applied as clinical hemoperfusion absorbent, was also used as a reference absorbent for comparison (Fig. S9). Fig. 3a shows the curve of VB12 and LYZ concentration with time of adsorption. When 2 mg MXene nanosheets were added into 4 mL VB12 solution (201.7 mg/L) at the temperature of 37 °C, the concentration of VB12 decreased rapidly to 122.6 mg/L in 30 min and then reached 90.3 mg/L after 3 h. In contrast, the concentration of VB12 only decreased to 171.1 mg/L after 3 h when using AC as the adsorbent. The $Ti_3C_2T_x$ MXene also displays superior removal capability for LYZ toxin. As shown in Fig. 3b, when 2 mg of MXene powders were mixed with LYZ aqueous dispersion, the concentration of LYZ dropped from 40.00 mg/L to 27.65 mg/L in 30 min and attained 21.60 mg/L after 3 h, while the concentration of LYZ treated with AC sorbent only attained 29.75 mg/L by the AC. To achieve a quantitative comparison between removal abilities of two absorbent, adsorption capacity q was quantified and calculated by the

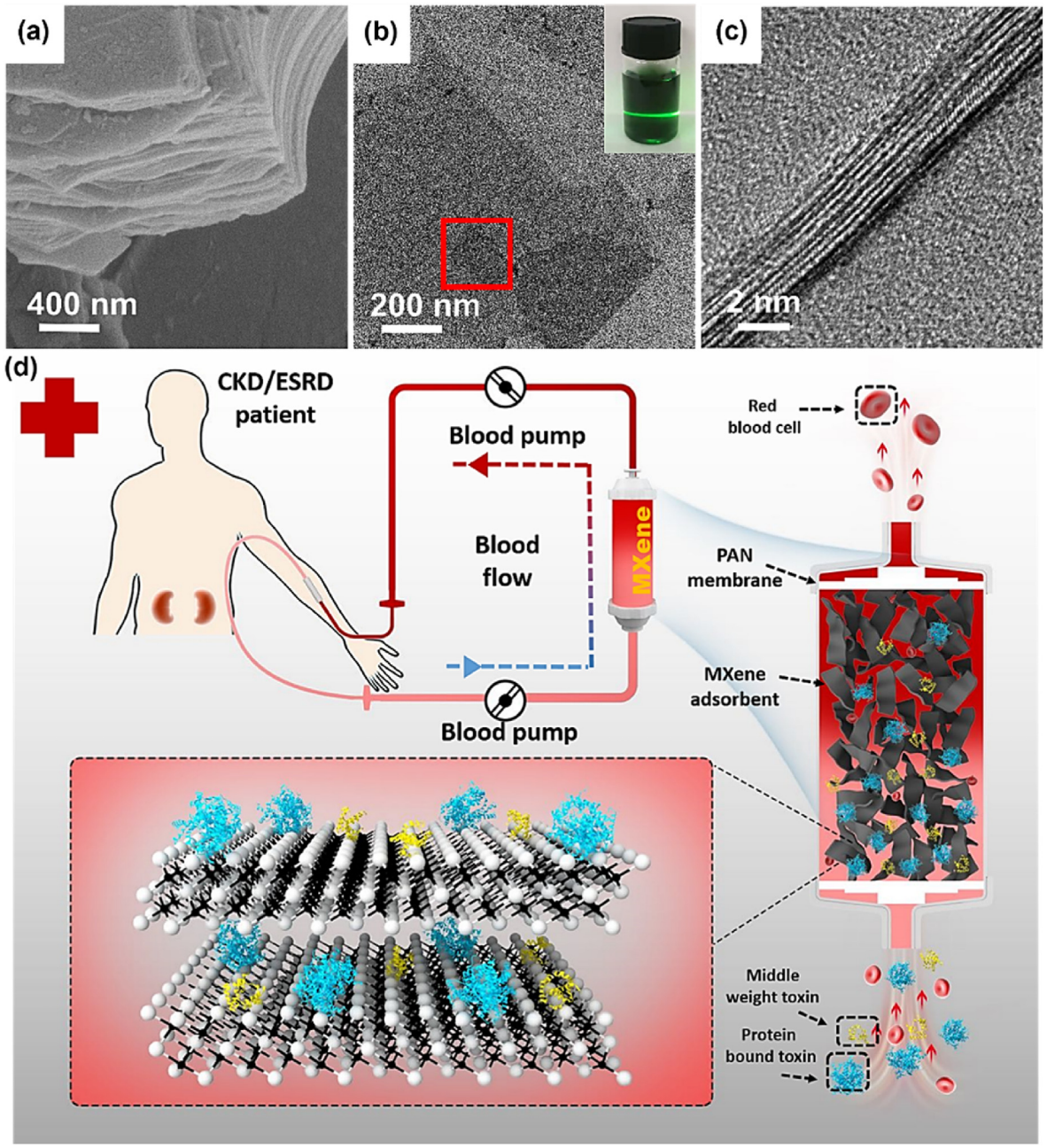

Fig. 1. (a) SEM image of $Ti_3C_2T_x$ MXene material after etching by HF. (b) TEM image of few-layer $Ti_3C_2T_x$ MXene material after delamination. The inset is a digital photograph of an aqueous dispersions of few-layer $Ti_3C_2T_x$, which shows the typical Tyndall effect. (c) HR-TEM image of $Ti_3C_2T_x$ MXene and the corresponding atomic model. (d) Schematic illustration of the hemoperfusion therapy process and mechanism by using the 2D MXene adsorbent.

formula below:

$$q = \frac{(c_t - c_o)V}{m_{ads}} \quad (1)$$

where c_o and c_t are the solute concentrations in the original solution and after a time t, respectively. V is the volume of solution and m_{ads} stands for the mass of sorbent. As showed in Fig. 3c, MXene showed a high VB12 adsorption capacity above 200 mg/g in mono-toxin solution and 120.1 mg/g in the mixed solution. However, in a sharp contrast, the adsorption capacity of AC ($D_H = 0.8$ mm, specific surface area is 800 m^2/g) to VB12 is only half of that of MXene in a mixed solution even in a mono toxin solution (61.2 mg/g). Besides to VB12, MXene also exhibited nearly double adsorption capacity (36.8 mg/g) than that of AC (20.5 mg/g) in mono toxin solution and almost triple in mixed toxin solution. The decreased performance in mixed solutions can be ascribed to the adsorption competition mechanism. Even compared with another commercial adsorbent, resin ($D_H = 205$ nm, Polydispersity index from cumulant fitting is 0.041, Average hydrodynamic diameter is 215 nm), MXene is still advantageous to toxin absorption (resin only achieved an adsorption ability of 13.3 mg/g, which is just one-third of the value of the MXene) [33]. Fig. 3e and f illustrate adsorption capacity of MXene and AC towards two typical small molecular weight toxins (urea and uric acid) in mono- and mix-toxin aqueous. Compared with AC, the adsorption capacity of MXene is higher than that of AC by more

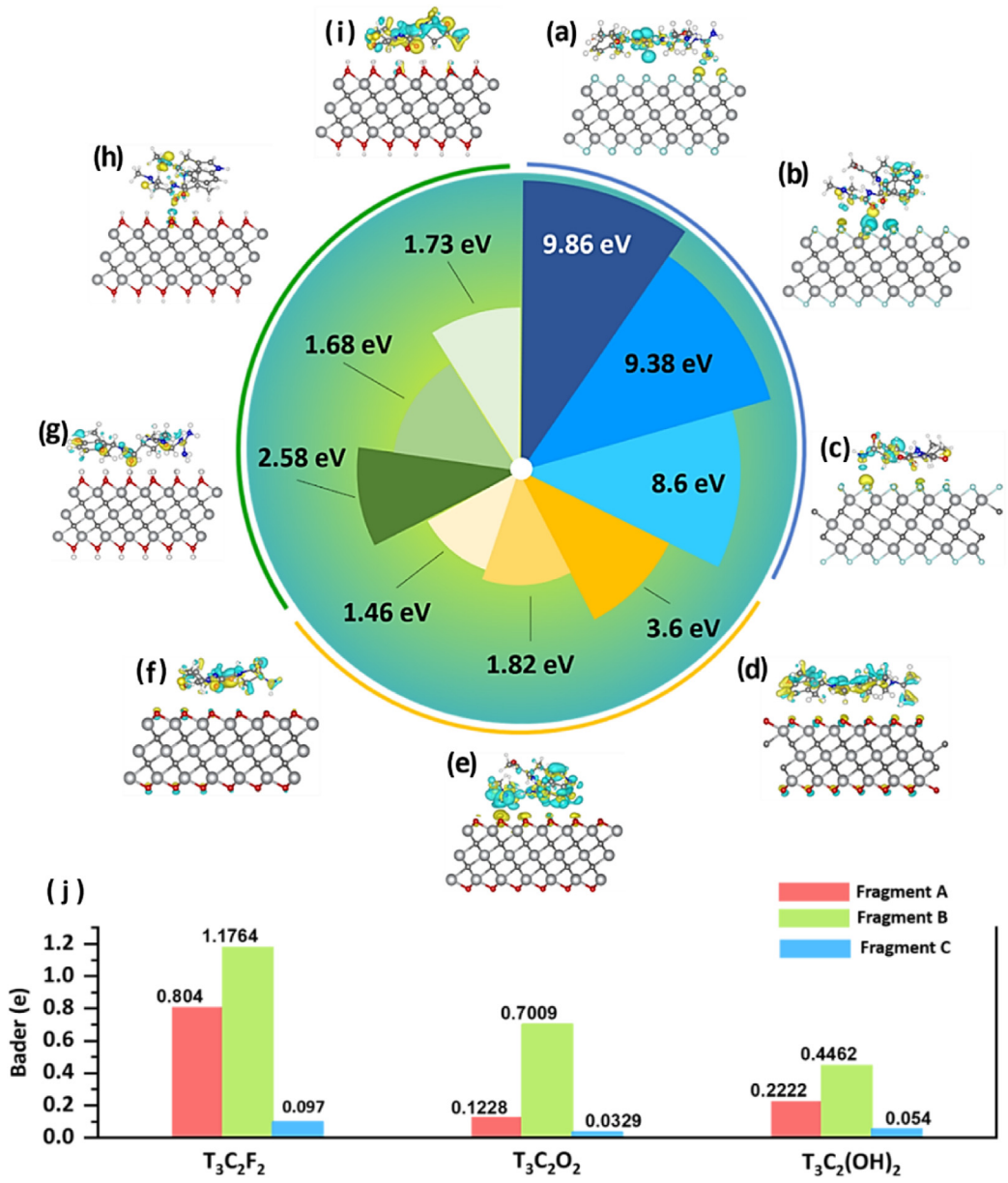

Fig. 2. Schematic illustration and computation on the interactions between $Ti_3C_2T_x$ MXene and LYZ segments. Blue, yellow and green sectors represent binding energies between (a–c) –F, (d–f) –O– and (g–i) –OH terminated MXene and three different LYZ segments A, B and C, respectively. The area of sectors corresponds to the strength of the binding energies they represent. (j) Bader charges for protein segments A, B and C with MXene terminated by three different functional groups.

50% in both solutions, which confirm a higher efficient removal efficiency for small molecular weight toxins. However, this excellent adsorption capability is dwarfed when compared with that of middle molecular mass and protein bound toxins. These results demonstrate the advances of $Ti_3C_2T_x$ MXene for absorbing small molecular mass, middle molecular mass, or protein bound toxins compared with conventional AC and resin absorbents [34,35]. We further examined the correlations between the quantity of absorbents and the removal efficiencies by adjusting the adsorbent mass loadings. Fig. 3g shows the removal efficiencies of MXene and AC to VB12 and LYZ when the mass loadings increased from 4 g to 10 g. In general, the adsorption capacities have been improved along with the increasing amounts of adsorbents. However, the growth of efficiencies when using MXene is much faster compared to using AC. Particularly, the remove efficiency gap between employing MXene and AC enlarged with the increase of absorbent loading. When the loading mass was 2.0 g, the removal efficiencies of MXene to VB12 and lysozyme were both close to 99%. While AC only achieved 57.4% and 43.7%, respectively. Furthermore, the adsorption rate of MXene for uric acid, VB12 and LYZ is much higher than that of AC, reflecting by the higher slopes in Fig. 3d-f. For clinical hemoperfusion, the adsorption rate is critically important to the therapeutic effect because blood usually only stays in the hemoperfusion column for a short time [34]. To simulate a realistic hemoperfusion process, we employed 3D printing technology to assemble a mini-module of the hemoperfusion column (Fig. 3h). 150 mg MXene/AC absorbent was tightly compacted on a polyacrylonitrile (PAN) membrane to prevent sorbent materials from escaping in the mini column. When the syringe was slowly propelled, the VB12 solution flowed through the hemoperfusion column model. Fig. 3i displays the conformational architecture of the hemoperfusion column. The extremely obvious colour contrast revealed the excellent adsorbing ability of

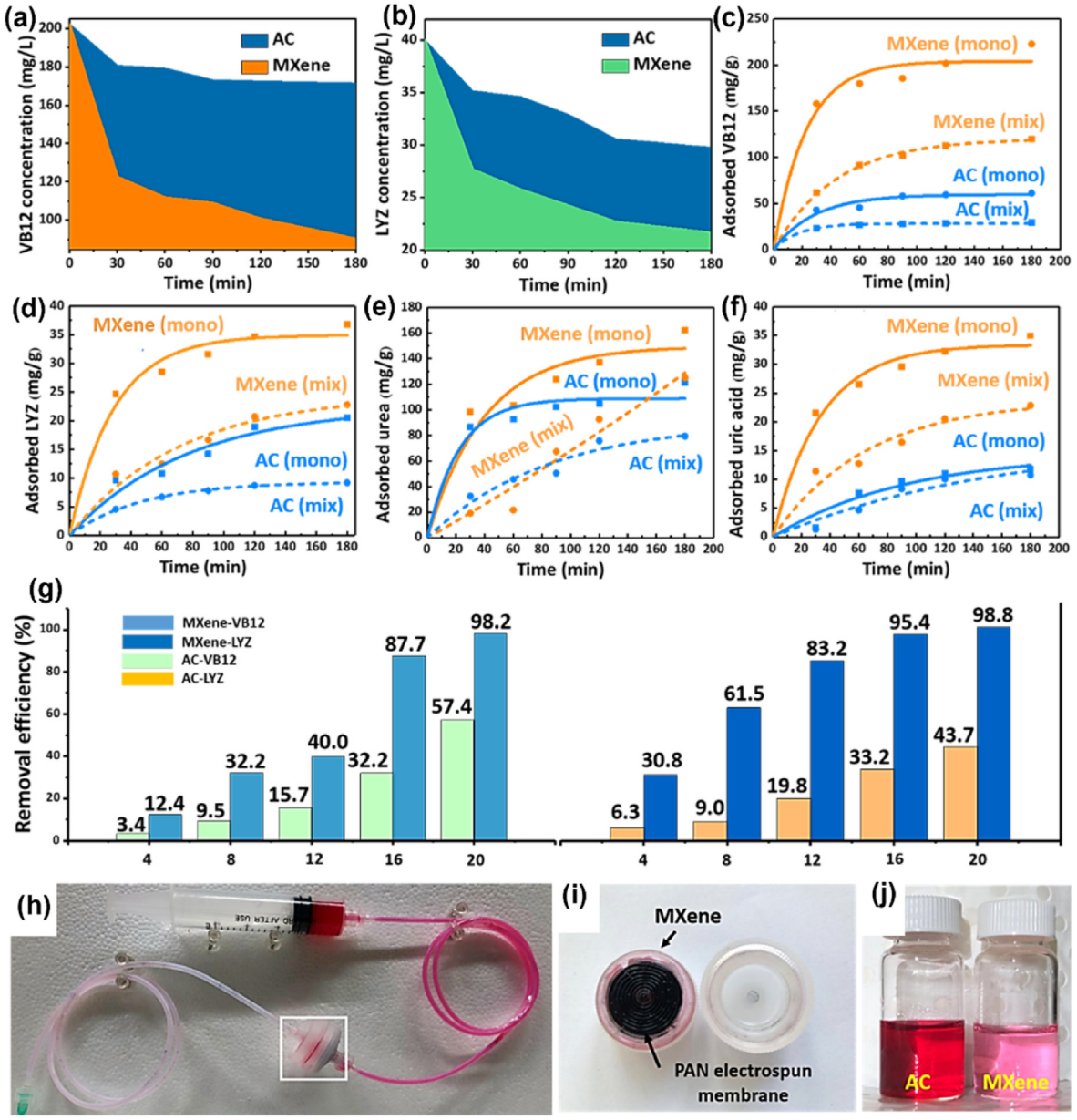

Fig. 3. Adsorption performance of MXene towards toxin or their representative. Comparison of MXene's and AC's time-concentration curve for (a) VB12 and (b) LYZ. Comparison of MXene's and AC's time-adsorb capacity curve for (a) VB12, (b) LYZ acid, (c) urea and (d) uric acid in mono- and mixed solution. (g) Comparison of MXene's and AC's removal efficiency of LYZ and VB12 by MXene or AC with varied mass loadings in aqueous solution. (h) Mini hemoperfusion Column. (i) A detailed configuration of simulated hemoperfusion column. (j) Comparison of purified VB12 solution through mini hemoperfusion Column containing AC and MXene absorbent.

MXene. Fig. 3j shows the VB12 solution after the absorption of AC and MXene, clearly indicating that MXene has much stronger adsorption ability than that of AC.

3.3. Adsorption mechanism of MXene towards toxins

To unravel the mechanism underpinning the highly efficient adsorption performance of MXene towards toxins, we performed systematic investigations on the adsorbent before and after adsorbing toxin molecules. Fig. 4a shows that MXene nanosheets were covered by a thick layer of coral-like LYZ when immersed in low concentration LYZ solution (0.01 g/L) for 3 min. When magnify the bridge section between LYZ and MXene, it can be found that LYZ inclined to attach to the edge of MXene with large curvature (Fig. 4b). Additionally, the adsorbed LYZ is more convergent and integrated into small spheres (Fig. 4c). Fig. 4d illustrates the border lines between the adsorbed LYZ and MXene nanosheet. Obviously, the adsorption of LYZ at both edges of the MXene nanosheet is much higher than that in the middle region. However, when the concentration was increased, the adsorption behaviour is quite different. As shown in Fig. 4e, when MXene absorbents were immersed in high concentration LYZ solution (0.15 g/L), they were instantaneously grafted by numerous LYZ "grapes" (clots), referred to as the "Cooperative effect." These clot spheres with an average diameter of 100 nm are self-induced aggregation of LYZ (Fig. 4f and g), which is consistent with the previous observations [35]. Upon immersed in an environment with abundant protein, the nanoparticles' (NPs) surfaces will rapidly be covered by successive sets of protein, forming a so-called "protein corona" [36]. Nevertheless, the density of these clots at the edge of MXene flakes are still much

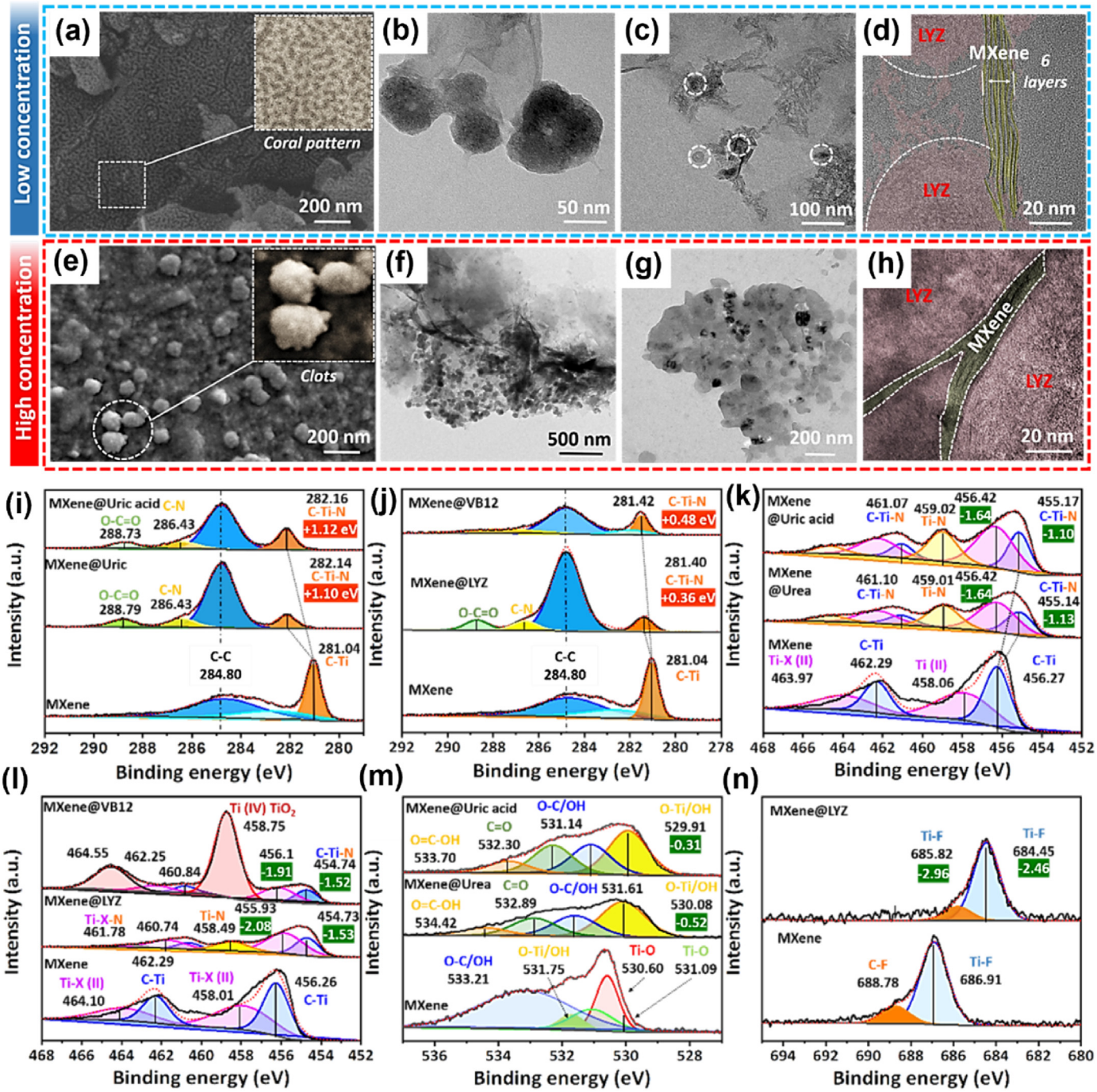

Fig. 4. Postmortem analysis for the MXene after adsorbed toxins. STEM and HR-TEM characterizations of MXene absorbent after immersed in (a–d) low concentrated (0.01 g/L) and (e–h) high concentrated (0.15 g/L) LYZ solution. (i and j) C1s XPS spectrum of MXene before and after adsorbing urea, uric acid, VB12 and LYZ. (k and l) Ti 2*p* XPS spectrum of MXene before and after adsorbing urea, uric acid, LYZ and VB12. (m) O 1s XPS spectrum of MXene before and after adsorbing uric acid and urea. (n) F 1s XPS spectrum of MXene before and after adsorbing LYZ.

higher than that at other regions of MXene nanosheets.

For most proteins, their Hill coefficients *n* are above 1 in the size span of 5–100 nm, which is exactly the size range of MXene absorbent particles [37]. According to the research reported by Cederavall *et al.*, there was a distinct difference in the degree of protein surface coverage of NPs depending on their size, with a larger degree of protein coverage on larger particles [38]. With the cooperative binding effect and "Vroman effect" [39]. The adsorption ability of LYZ@MXene to the later arriving LYZ was accelerated, and enhanced and the whole "protein corona" grown bigger like a rolling snow ball. Fig. 4h illustrates internal details of one LYZ clot where LYZ (colored red) accumulation has become saturated and the core of which is a piece of MXene nanosheet (colored yellow). Fig. S10 reveals a magnified feature of clots dotted along the edge of few-layer MXene nanosheets and EDS was employed to further analyze the distribution of LYZ on MXene sorbent. The presence of N element indicates the existence of LYZ molecules. Additionally, all elements signals in the edge region (labelled by the white dashed

line) are stronger than that in the flat region. Klein et al. claimed that the curvature of smaller NPs may entirely affect the adsorption of certain proteins, especially for large or less conformationally flexible proteins; Therefore, both the NP size and surface composition are very important parameters in defining the composition of the formed protein corona [40]. Except for the curvature of particles, surface roughness [41] and surface defect [42] also greatly minimized repulsive interaction, thereby promoting adhesion of protein to the NPs. The shape of NP has a great impact not only on its physiochemical characteristic but also on the way that proteins adsorb onto its surface and consequently on the way that protein interacts with it [43]. According to analysis on the structure of clot, we can conclude that the LYZ absorbed on MXene is multilayered, which is quite different from traditional chemical or physical adsorption (AC or resin, *etc.*). This also explains why MXene absorbent delivered a much higher adsorption capacity that of AC.

XPS analysis was performed to investigate the chemisorptive nature and affinity between the MXene sorbent and toxin molecules. As shown in Fig. S11, the presence of N 1*s* peaks in the post-treated MXene indicates the successful adsorption of toxins. Fig. 4i and j show high-resolution XPS C 1*s* spectrum of MXene after adsorption of urea, uric acid, VB12 and LYZ, which are denoted as MXene@toxins, respectively. The peak corresponding to the C—Ti bond shifted from 281.04 eV to 282.16 eV, 282.14 eV, 282.42 eV and 281.40 eV after adsorbing urea, uric acid, VB12 and LYZ, respectively. The positive shifts of peaks (+1.12, +1.10, +0.48 and + 0.36 eV) can be ascribed to the formation of the C—Ti—N bond [44,45]. This result demonstrates that the amino or peptide moieties of toxins can chemically bond with Ti atoms of MXene. The increased peak intensity of C—C bond, and the appearance of C—N bond and C=O bond peaks further confirm the successful adsorption of the toxin molecules [46]. In the Ti 2*p* spectrum, shifts of −1.10, −1.13, −1.52 and −1.53 eV of the C—Ti peak can be observed in the XPS spectrum of MXene@toxins, which also verifies the effective adsorption of various toxins by the MXene (Fig. 4k and L). A new peak appearing at 458.75 eV corresponds to Ti (IV), which could be originated from the partial oxidization of MXene in contact with oxidant VB12. However, the oxidation was not observed in other MXene absorbed toxins, and the negative shifts Ti (II) peak by −1.64, −1.64, −1.91 and −2.08 eV corresponding to the hydrogen bond formation in the form of Ti—X … H—N (X is −F, −O− or OH−). This phenomenon shows that the N-containing functional groups (−OC−NH−, $-ONH_2$ *etc.*) can form hydrogen bonds with −OH, −O− and −F functional groups on the surface of MXene adsorbents [47]. We suggested that the surface functional groups and hydrogen bond play a key role in alleviating protein bound toxins from their large steric hindrance. The Ti—F and C—F peaks at 685.2 eV and 687.04 eV, shift to 684.45 eV and 685.8 eV after adsorbing LYZ **(**Fig. 4n**)**, which can also be ascribed to hydrogen bonds between F- functional and peptide bonds. This kind of strong adsorption is also reflected in the O 1*s* where MXene adsorbs urea and uric acid (Fig. 4m). The interactions between MXene and VB12 or LYZ were also investigated by Fourier transform infrared spectroscopy (FT-IR). Fig. S12 shows FT-IR spectrum of MXene, urea, uric acid, LYZ, VB12 and their combination. It can be observed that either the characteristic peaks of MXene functional group or the characteristic peaks of the toxin molecule basically disappeared after adsorbing toxins, which is in accordance with the XPS analysis results [48].

To further investigate the mechanism of MXene for persistent adsorption of protein bound toxins, we conducted the measurement of circular dichroism (CD) spectroscopy, FTIR characterization and nuclear magnetic resonance (NMR) to analyze the structural changes of LYZ after adsorbed by MXene [49,50]. Fig. 5a shows the CD spectra of LYZ before and after immobilization on MXene sorbent. The pristine LYZ shows a double negative peak at 217 nm and 211 nm, and a negative peak at 195 nm, which are signatures of an α-helix structure [51,52]. However, after immobilized by MXene, the CD spectrum of LYZ transformed into a single peak between 210 and 225 nm and a positive peak between 190 and 200 nm. This change indicates the secondary structure of LYZ molecules transformed to β-sheet dominated structure [53,54]. This transformation of secondary structure of LYZ is also verified by the FTIR characterization (Fig. 5b). The structural change was mainly found in the Amide I area (from 1 700 to 1 600 cm^{-1}), which is often utilized to identify proteins' secondary structure. The pristine LYZ has two characteristic peaks at 1 637 and 1 501 cm^{-1}, which are shifted to 1 611 and 1 494 cm^{-1} after the adsorption by MXene, corresponding to the secondary structural transformation of LYZ [55]. The irreversible denaturation of LYZ was also monitored by one dimensional ^{1}H NMR [56]. In Fig. 5c, the high-field region of the spectrum (from 4.5 to −2.0) is dominated by the signals of the aliphatic groups of the protein molecule. While the signals in low-field region corresponds to the aromatic residues (from 8 to 6) and amide protons (from 10 to 8) [57]. It is noted that both the half peak width and peak intensity of immobilized LYZ at the region of ~8.3 are enhanced compared with pristine LYZ, which also confirms the secondary structural transformation of the LYZ molecules. Additionally, some new peaks (labelled by red triangles) appear in the MXene immobilized LYZ, which are typical signal associated with secondary structural shift of proteins [58].

By comparing the structural transformation of LYZ adsorbed on MXene, we can further understand the mechanism why MXene is capable to remove protein bound toxins more efficiently. As shown in Fig. 5d, when protein bound toxins such as LYZ interact with MXene nanosheets. The peptide bonds in proteins can form strong chemical bonds with the surface functional groups of MXene. Assisted with amphiphilicity of MXene surface (1/2 −F and 1/2 O contained terminal groups), this strong affinity conjoining with "Electrostatic effect" and hydrophobic effects between MXene and protein, induce the transformation of the secondary structure of protein from an α-helix to a β-sheet [59]. Since β-sheet structure is more stable and less soluble than that of α-helix, therefore, those toxin molecules are firmly immobilized on the surface of MXene. Furthermore, because of the "Cooperative binding effect", the first-come protein can largely accelerate the adsorption and folding of latter arriving protein molecules [60]. Particularly, protein bound toxins are preferentially adsorbed at the sharp edges and corners of the absorbent for immobilization.

3.4. Effect of MXene on toxin remove and other components of blood

To understand the effect of MXene on toxin remove and other components of blood in real hemoperfusion, we used the real blood of an ESRD patient to simulate the adsorption difference between MXene and commercial AC absorbents. As shown in Fig. 5e, when 2 mg MXene and AC absorbents were added into real blood separately, MXene showed better removal efficiencies towards toxin molecules such as urea (2.52%), uric acid (22.14%) and β_2-microglobulin (15.99%) than that of AC (urea (1.8%), uric acid (18.73%) and β_2-microglobulin (12.23%)). In addition, through comparing the concentration of various anions in the blood of patients after blood adsorption, we found that the clearance ratio of MXene to P, K, Cl ions was lower than that of AC, except for Na ions. These results indicate that MXene has a smaller side effects on the charge balance and osmotic pressure in the blood compared to AC sorbent. Furthermore, we found that MXene would not significantly decrease the concentration of beneficial proteins in human blood. The clearance ratio of MXene to albumin (ALB) is the same as that of

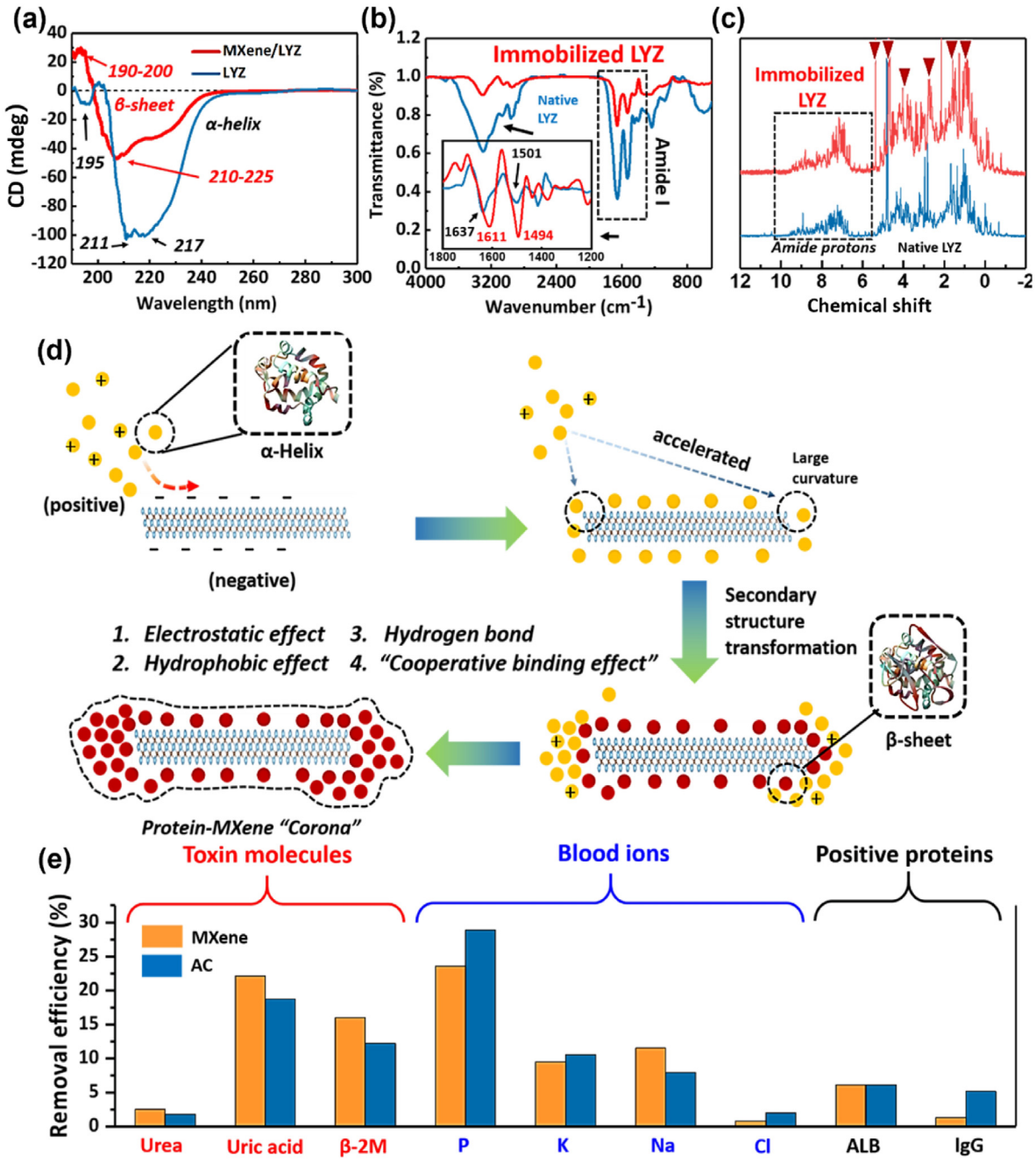

Fig. 5. (a) CD spectra of LYZ before and after immobilization on MXene nanosheets. (b) FT-IR results of LYZ before and after absorption on MXene. The inset in the curve is Amide I treated by a first differential procession. (c) 1D ^{1}H NMR spectrum comparison of LYZ before and after being adsorbed on MXene nanosheets. The inset is a close-up of features in the area near 8.3×10^{-6}. (d) Schematic diagram of secondary structural transformation illustrated by "Corona" module. (e) Comparison of removal rate of different components in whole blood experiment of ESRD patients with MXene.

AC, while the removal ratio to immunoglobulin G (IgG) is much lower. ALB and IgG both are important positive proteins in human plasma. ALB functions primarily as a carrier protein for steroids and fatty acids in the blood and plays a major role in stabilizing extracellular fluid volume by contributing to osmotic pressure [57]. IgG is the main type of antibody controlling infection of body tissues [60,61]. The low removal ability of MXene towards these two beneficial proteins also protects patients from the side effects of the hemoperfusion process, hence benefiting the recovery of ESRD patients.

3.5. Hemoperfusion process simulation

To further understand the effect of MXene absorbents on blood during the real hemoperfusion process, we employed a healthy goat for an *in vivo* hemoperfusion simulation experiment (as shown in Fig. 6a). The blood samples collected at the outlet of the perfusion column confirm that after the MXene adsorption, all parameters of blood have not changed greatly and remain within a reasonable range (Fig. 6b). More importantly, as demonstrated in Fig. 6c and d, when comparing the blood sample taken from the goat 4 h after the completion of the hemoperfusion experiment and

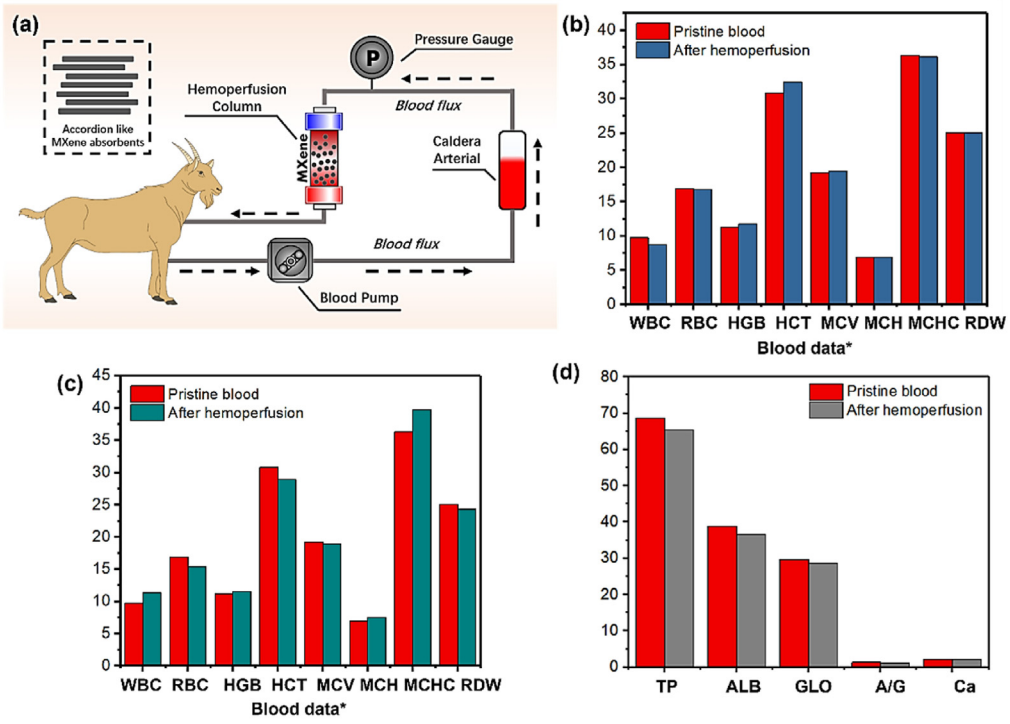

*Full name of blood data

Blood data	Full name	Unit
WBC	White blood cell count	$\times 10^{9}$ L^{-1}
RBC	Red blood cell count	$\times 10^{12}$ L^{-1}
HGB	Hemoglobin	×10 g/L
HCT	Red blood cell specific volume	%
MCV	Blood mean red cell volume	fL
MCH		pg
MCHC	Mean corpuscular hemoglobin concentration	×10 g/L
RDW	Red cell distribution wideth	%
TP	Total protein	g/L
ALB	Albumin	g/L
GLO	Globulin	g/L
A/G	Albumin/ Globulin	
Ca^{2+}	Calcium ion	mol/L

Fig. 6. (a) *In vivo* evaluation for blood compatibility of MXene absorbents through health goat whole blood hemoperfusion. (b) Comparison demonstrates variation of different typical components of pristine, after adsorption of MXene absorbent. (c) Comparison demonstrates variation of different typical components of boat blood sample taken 4 h after MXene hemoperfusion treatment. (d) Comparison of plasma protein and ions of goat blood before and after MXene hemoperfusion.

the pristine blood sample, it can be found that the goat blood data are all kept within a reasonable range without any significant differences. This experiment further confirms the good hemocompatibility and safety of MXene absorbents to blood [62,63].

4. Conclusion

In conclusion, we discovered that MXene material can adsorb small-, middle-molecular weight and protein-bound toxins for hemoperfusion with ultrahigh efficiencies. DFT computations and XPS analyses indicated that both Ti and the surface functional groups in MXene possess strong chemical binding affinities towards uremic toxin molecules. Furthermore, CD spectroscopy, FTIR and 1D ^{1}H NMR measurement results comprehensively revealed that protein bound toxin molecules were denatured *via* the transformation of their secondary structure from α-helix to β-sheets after adsorbed by MXene, which effectively improve the adsorption capacity of MXene absorbent. The high adsorption efficiency of MXene for the removal of middle-molecular weight and protein bound toxins perfectly fills the gap between traditional hemodialysis and hemoperfusion. The adsorption test using blood from ESRD patients confirmed that MXenes are better absorbents than AC as they can remove most uremic toxins without causing much negative effects on other positive components in the blood.

This work sheds light on the development of new absorbent materials for removal uremic toxins with ultrahigh efficiency. Furthermore, MXene absorbent could also be potentially used for in hemoperfusion for the treatment of sever COVID-19 patients to remove interleukin-6 toxins generated by “cytokine storm”.

Declaration of competing interest

The authors declare that they have no known competing financial interests or personal relationships that could have appeared to influence the work reported in this paper.

Acknowledgements

T. W. would like to acknowledge support of National Natural Science Foundation of China (NO. 22102141). H.Y. would like to acknowledge the financial support of the “Young scientists lifting project” of Jiangsu Province, China (TJ-2022-072). The test Centre of Yangzhou University provided the facilities for SEM, TEM, CD spectroscopy and XPS measurements.

Appendix A. Supplementary data

Supplementary data to this article can be found online at https://doi.org/10.1016/j.jmat.2023.06.010.

References

[1] Centers for Disease Control and Prevention. Chronic kidney disease surveillance system-United States. http://www.cdc.gov/ckd. [Accessed 11 March 2023].
[2] Reynolds JL, Joannides AJ, Skepper JN, McNair R, Schurgers LJ, Proudfoot D, et al. Human vascular smooth muscle cells undergo vesicle-mediated calcification in response to changes in extracellular calcium and phosphate concentrations: a potential mechanism for accelerated vascular calcification in ESRD. J Am Soc Nephrol 2004;15:2857–67. https://doi.org/10.1097/01.ASN.0000141960.01035.28.
[3] Levey AS, Coresh J. Chronic kidney disease. Lancet 2012;379:165–80. https://doi.org/10.1016/S0140-6736(11)60178-5.
[4] El Nahas AM, Bello AK. Chronic kidney disease: the global challenge. Lancet 2005;365:331–40. https://doi.org/10.1016/S0140-6736(05)17789-7.
[5] Lin W, Liu T, Yang M. Hemocompatibility of polyacrylonitrile dialysis membrane immobilized with chitosan and heparin conjugate. Biomaterials 2004;25:1947–57. https://doi.org/10.1016/j.biomaterials.2003.08.027.
[6] Vanholder R, De Smet R, Glorieux G, Argilés A, Baurmeister U, Brunet P, et al. Review on uremic toxins: classification, concentration, and interindividual variability. Kidney Int 2003;63:1934–43. https://doi.org/10.1046/j.1523-1755.2003.00924.x.
[7] Winchester JF. Dialysis and hemoperfusion in poisoning. Adv Ren Replace Ther 2002;9:26–30. https://doi.org/10.1053/jarr.2002.30470.
[8] Ronco C, Reis T, De Rosa S. Coronavirus epidemic and extracorporeal therapies in intensive care: si vis pacem para bellum. Blood Purif 2020;49:255–8. https://doi.org/10.1159/000507039.
[9] Naguib M, Kurtoglu M, Presser V, Lu J, Niu J, Heon M, et al. Two-dimensional nanocrystals produced by exfoliation of Ti_3AlC_2. Adv Mater 2011;23:4248–53. https://doi.org/10.1002/adma.201102306.
[10] Ghidiu M, Lukatskaya MR, Zhao MQ, Gogotsi Y, Barsoum MW. Conductive two-dimensional titanium carbide 'clay' with high volumetric capacitance. Nature 2014;516:78–81. https://doi.org/10.1038/nature13970.
[11] Xue Q, Zhang H, Zhu M, Pei Z, Li H, Wang Z, et al. Photoluminescent Ti_3C_2 MXene quantum dots for multicolor cellular imaging. Adv Mater 2017;29:1604847. https://doi.org/10.1002/adma.201604847.
[12] Shahzad F, Alhabeb M, Hatter CB, Anasori B, Hong SM, Koo CM, et al. Electromagnetic interference shielding with 2D transition metal carbides (MXenes). Science 2016;353:1137–40. https://doi.org/10.1126/science.aag2421.
[13] Naguib M, Mochalin V, Barsoum M, Gogotsi Y. 25th anniversary article: MXenes: a new family of two-dimensional materials. Adv Mater 2014;26:992–1005. https://doi.org/10.1002/adma.201304138.
[14] Zhang Q, Teng J, Zou G, Peng Q, Du Q, Jiao T, et al. Efficient phosphate sequestration for water purification by unique sandwich-like MXene/magnetic iron oxide nanocomposites. Nanoscale 2016;8:7085–93. https://doi.org/10.1039/C5NR09303A.
[15] Naguib M, Mashtalir O, Carle J, Presse V r, Lu J, Hultman L, et al. Two-dimensional transition metal carbides. ACS Nano 2012;6:1322–31. https://doi.org/10.1021/nn204153h.
[16] Wang H, Zou W, Liu C, Sun Y, Xu Y, Sun W, et al. β-ketoenamine-linked covalent organic framework with Co Intercalation: Improved lithium-storage properties and mechanism for high-performance lithium-organic batteries. Batteries & Supercaps 2022;6:e202200434. https://doi.org/10.1002/batt.202200434.
[17] Chen X, Zhang H, Ci C, Sun W, Wang Y. Few-layered boronic ester based covalent organic frameworks/carbon nanotube composites for high-performance K-organic batteries. ACS Nano 2019;13:3600–7. https://doi.org/10.1021/acsnano.9b00165.
[18] Zhang Y, Wang Y, Guo C, Wang Y. Molybdenum carbide-based photocatalysts: synthesis, functionalization, and applications. Langmiur 2022;38:12739–56. https://doi.org/10.1021/acs.langmuir.2c01887.
[19] Guo Z, Li Y, Sa B, Fang Y, Lin J, Huang Y, et al. M_2C-type MXenes: Promising catalysts for CO_2 capture and reduction. Appl Surf Sci 2020;521:146436. https://doi.org/10.1016/j.apsusc.2020.146436.
[20] Liu N, Ma S, Jiao Z. MXene V_2CO_2 monolayer : a promising adsorbent to capture toxic NH3 gas. Physica E Low Dimens 2023;148:115651. https://doi.org/10.1016/j.physe.2023.115651.
[21] Yu S, Tang H, Zhang D, Wang S, Qiu M, Song G, et al. Sci Total Environ 2022;811:152280. https://doi.org/10.1016/j.scitotenv.2021.152280.
[22] Hwang S, Kang S, Rethinasabapathy M, Roh C, Huh Y. Chem Eng J 2020;397:125428. https://doi.org/10.1016/j.cej.2020.125428.
[23] Meng F, Seredych M, Chen C, Gura V, Mikhalovsky S, Sandeman S, et al. MXene sorbents for removal of urea from dialysate: a step toward the wearable artificial kidney. ACS Nano 2018;12:10518–28. https://doi.org/10.1021/acsnano.8b06494.
[24] Wang T, Sun X, Guo X, Zhang J, Yang J, Tao S, et al. Ultraefficiently calming cytokine storm using $Ti_3C_2T_x$ Mxene. Small Methods 2021;5:2001108. https://doi.org/10.1002/smtd.202001108.
[25] Sun X, Yang J, Su D, Wang C, Wang G. Highly efficient adsorption of bilirubin by $Ti_3C_2T_x$ Mxene. Chem Asian J 2021;16:1949–55. https://doi.org/10.1002/asia.202100332.
[26] Kresse G, Furthmüller J. Efficiency of ab-initio total energy calculations for metals and semiconductors using a plane-wave basis set. Comput Mater Sci 1996;6:15–50. https://doi.org/10.1016/0927-0256(96)00008-0.
[27] Kresse G, Hafner J. Ab initio molecular dynamics for open-shell transition metals. Phys Rev B 1993;48:13115–8. https://doi.org/10.1103/PhysRevB.48.13115.
[28] Perdew JP, Burke K, Ernzerhof M. Generalized gradient approximation made simple. Phys Rev Lett 1997;78(1396):96. https://doi.org/10.1103/PhysRevLett.78.1396.
[29] Blöchl PE. Projector augmented-wave method. Phys Rev B 1994;50:17953–79. https://doi.org/10.1103/PhysRevB.50.17953.
[30] Liu X, Gong Q, Zhao M, Bai J, Huang Y, Gan J, et al. Preparation of Na-alginate/CNTs composite spheres by dripping-gelatinization process and their enhanced adsorption of VB_{12} by freeze-casting. J Porous Mater 2019;26:353–60. https://doi.org/10.1007/s10934-018-0607-2.
[31] Monkhorst HJ, Pack JD. Special points for Brillouin-zone integrations. Phys Rev B 1976;13:5188–92. https://doi.org/10.1103/PhysRevB.13.5188.
[32] Oksanen V, Grönhagen-Riska C, Tikanoja S, Somer H, Fyhrquist F. Cerebrospinal fluid lysozyme and beta 2-microglobulin in neurosarcoidosis. J Neurol Sci 1986;73:79–87. https://doi.org/10.1016/0022-510x(86)90066-3.
[33] Wibell L, Evrin PE, Berggard I. Serum 2-microglobulin in renal disease. Nephron 1973;10:320–31. https://doi.org/10.1159/000180203.
[34] Sun L, Yan P, Zhang Y, Wei L, Li G. Effect of activated charcoal hemoperfusion on renal function in patients with paraquat poisoning. Exp Ther Med 2018;15:2688–92. https://doi.org/10.3892/etm.2018.5712.
[35] Barhoum S, Yethiraj A. An NMR study of macromolecular aggregation in a model polymer-surfactant solution. J Phys Chem B 2010;114:17062–7. https://doi.org/10.1063/1.3290985.
[36] Monopoli MP, Walczyk D, Campbell A, Elia G, Lynch I, Bombelli FB, et al. Physical-chemical aspects of protein corona: relevance to in vitro and in vivo biological impacts of nanoparticles. J Am Chem Soc 2011;133:2525–34. https://doi.org/10.1021/ja107583h.
[37] Mahmoudi M, Lynch I, Ejtehadi MR, Monopoli MP, Bombelli FB, Laurent S. Protein-nanoparticle interactions: opportunities and challenges. Chem Rev 2011;111:5610–37. https://doi.org/10.1021/cr100440g.
[38] Cedervall T, Lynch I, Lindman S, Berggård T, Thulin E, Nilsson H, Dawson KA, et al. Understanding the nanoparticle–protein corona using methods to quantify exchange rates and affinities of proteins for nanoparticles. Pro Nati Acad Sci 2007;104:2050–5. https://doi.org/10.1073/pnas.0608582104.
[39] Horbett TA, Brash JL. ACS symposium series, 602. Washington DC: American Chemical Society; 1995. p. 112–28.
[40] Klein J. Probing the interactions of proteins and nanoparticles. Pro Nati Acad Sci 2007;104:2029–30. https://doi.org/10.1073/pnas.0611610104.
[41] Nel AE, Mädler L, Velegol D, Xia T, Hoek EMV, Somasundaran P, et al. Understanding biophysicochemical interactions at the nano-bio interface. Nat Mater 2009;8:543–57. https://doi.org/10.1038/nmat2442.
[42] Näreoja T, Määttänen A, Peltonen J, Hänninen PE, Härmä H. Impact of surface defects and denaturation of capture surface proteins on nonspecific binding in immunoassays using antibody-coated polystyrene nanoparticle labels. J Immunol Methods 2009;347:24–30. https://doi.org/10.1016/j.jim.2009.05.010.
[43] Cox M, Barnham KJ, Frenkiel T, Hoeschele JD, Mason A, He Q. Identification of platination sites on human serum transferrin using (13)C and (15)N NMR

spectroscopy. J Biol Inorg Chem 1999;4:621–31. https://doi.org/10.1007/s007750050386.
[44] Bao W, Liu L, Wang C, Choi S, Wang D, Wang G. Facile synthesis of crumpled nitrogen-doped MXene nanosheets as a new sulfur host for lithium–sulfur batteries. Adv Energy Mater 2018;8:1702485. https://doi.org/10.1002/aenm.201702485.
[45] Wen Y, Rufford T, Chen X, Li N, Lyu M, Dai L, et al. Nitrogen-doped $Ti_3C_2T_x$ MXene electrodes for high-performance supercapacitors. Nano Energy 2017;38:368–76. https://doi.org/10.1016/J.NANOEN.2017.06.009.
[46] Van de Lagemaat E, De Groot L, Van den Heuvel EGHM. Vitamin B12 in Relation to oxidative stress: a systematic review. Nutrients 2019;11:482–97. https://doi.org/10.3390/nu11020482.
[47] Kerber SJ, Bruckner JJ, Wozniak K, Seal S, Hardcastle S, Barr TL. The nature of hydrogen in X-ray photoelectron spectroscopy: general patterns from hydroxides to hydrogen bonding. J Vac Sci Technol A 1996;14:1314–20. https://doi.org/10.1116/1.579947.
[48] Gao XT, Xie Y, Zhu XD, Sun KN, Xie XM, Liu YT, et al. Ultrathin MXene nanosheets decorated with TiO_2 quantum dots as an efficient sulfur host toward fast and stable Li-S batteries. Small 2018;14:1802443. https://doi.org/10.1002/smll.201802443.
[49] Greenfield NJ. Using circular dichroism spectra to estimate protein secondary structure. Nat Protoc 2006;1:2876–90. https://doi.org/10.1038/nprot.2006.202.
[50] Lynch I, Dawson K, Linse S. Detecting cryptic epitopes created by nanoparticles. Sci STKE 2006;2006:pe14. https://doi.org/10.1126/stke.3272006pe14.
[51] Rittle J, Field M, Green M, Tezcan F. An efficient, step-economical strategy for the design of functional metalloproteins. Nat Chem 2019;11:434–41. https://doi.org/10.1038/s41557-019-0218-9.
[52] Tanaka F, Forster L, Pal PK, Rupley JA. The circular dichroism of Lysozyme. J Biol Chem 1975;250:6977–82. https://doi.org/10.1016/S0021-9258(19)41028-4.
[53] Hancock TJ, Hsu J. Simple method for sample temperature calibration in a 500 MHz NMR spectrometer useful for protein studies. Biotechnol Tech 1996;12:494–502. https://doi.org/10.1007/BF00161590.
[54] Knubovets T, Osterhout JJ, Klibanov AM. Structure of lysozyme dissolved in neat organic solvents as assessed by NMR and CD spectroscopies. Biotechnol Bioeng 1999;63:242–8. https://doi.org/10.1002/(SICI)1097-0290(19990420)63:2%3C242::AID-BIT13%3E3.0.CO;2-N.
[55] Cruz-Angeles J, Martínez L, Videa M. Application of ATR-FTIR spectroscopy to the study of thermally induced changes in secondary structure of protein molecules in solid state. Biopolymers 2015;103:574–84. https://doi.org/10.1002/bip.22664.
[56] Ueda T, Isakari Y, Aoki H, Yasukochi T, Masutomo S, Kawano K, et al. ^{1}H-NMR Study of the intramolecular interaction of a substrate analogue covalently attached to aspartic acid-101 in lysozyme. J Biochem 1991;109:690–8. https://doi.org/10.1093/oxfordjournals.jbchem.a123442.
[57] McDonald C, Phillips W, Glickson J. Nuclear magnetic resonance study of the mechanism of reversible denaturation of lysozyme. J Am Chem Soc 1971;93:235–46. https://doi.org/10.1021/ja00730a039.
[58] Hancock TJ, Hsu J. Simple method for sample temperature calibration in a 500 MHz NMR spectrometer useful for protein studies. Biotechnol Tech 1994;8:199–202. https://doi.org/10.1007/BF00161590.
[59] Sim ES, Yi GS, Je M, Lee Y, Chung YC. Understanding the anchoring behavior of titanium carbide-based MXenes depending on the functional group in Lisingle bondS batteries: a density functional theory study. J Power Sources 2017;342:64–9. https://doi.org/10.1016/j.jpowsour.2016.12.042.
[60] Patterson SD, Waldron M, Jeffries O. Chapter 13 - proteins and amino acids and physical exercise. In: Walrand S, editor. Nutrition and skeletal muscle. Elsevier B.V, Academic Press; 2019. p. 183–96. https://doi.org/10.1016/C2016-0-00256-5.
[61] Liu H, Moynihan KD, Zheng Y, Szeto G, Li A, Huang B, et al. Structure-based programming of lymph-node targeting in molecular vaccines. Nature 2014;507:519–22. https://doi.org/10.1038/nature12978.
[62] Sirac C, Herrera G, Sanders P, Batuman V, Bender S, Ayala M, et al. Animal models of monoclonal immunoglobulin-related renal diseases. Nat Rev Nephrol 2018;14:246–64. https://doi.org/10.1038/nrneph.2018.8.
[63] Karnam A, Rambabu N, Das M, Bou-Jaoudeh M, Delignat S, Käsermann F, et al. Therapeutic normal IgG intravenous immunoglobulin activates Wnt-β-catenin pathway in dendritic cells. Commun Biol 2020;3:96–118. https://doi.org/10.1038/s42003-020-0825-4.

Dr. Tianyi Wang received his Ph.D degree from University of Technology Sydney (UTS) in 2021. He is an Associate Professor in the College of Chemistry and Chemical Engineering, Yangzhou University (YZU). His research domain mainly focuses on MXenes, energy storage technologies, the design of hemoperfusion absorbents, biomaterials and functionalization of nanomaterials.

Dr. Hang Yao received his bachelor's degree and Ph. D. degree from South China University of Technology (China) in 2012 and 2018, respectively. He is now an Associate Professor in Yangzhou University (China). Over the past five years, he has been engaged in the design and synthesis of functional biomaterials used in tissue engineering, especially for 3D cell culture and tissue repair. His research interests focus on multifunctional materials based on hydrogels and nano-biomaterials applied in tissue reconstruction.

Prof. Xiuyun Zhang obtained her PhD degree from Southeast University of Condensed physics in 2010. From 2011 to 2013, she worked on the theory of nanomaterials in institute of Textiles and Clothing in Hong Kong Polytechnic University. Now she is a professor of college of physics science and technology in Yangzhou University and her current research is focused on the growth mechanism, structure, properties and applications of low dimensional nanomaterials. To date, she has published more than 100 high level journal papers in international academic journals.

Prof. Guoxiu Wang is the Director of the Centre for Clean Energy Technology and a Distinguished Professor (2012-Present) in the School of Mathematical & Physical Sciences, Faculty of Science, at University of Technology Sydney (UTS), Australia. Professor Wang is an expert in materials chemistry, electrochemistry, energy storage and conversion, and battery technologies. His research interests include lithium-ion batteries, lithium-air batteries, sodium-ion batteries, lithium-sulfur batteries, supercapacitors, hydrogen storage materials, fuel-cells, graphene and MXenes.